Highest Maximum Power Point of Radially Distant Inductively Coupled Power Receivers with Deep Submicron CMOS

Nan Xing, *Graduate Student Member, IEEE*, and Gabriel A. Rincón-Mora, *Fellow, IEEE*

***Abstract*— Inductively coupled power receivers for embedded microsensors are often tiny and distant from their transmitting sources. To sustain microsensors as long as possible, the power receiver should draw power whenever possible and output the highest power possible. Of reported state-of-the-art technologies, switched resonant half-bridges require fewer components, are less breakdown-limited, and output as much or more power than the others. This paper derives and shows with measurements the highest possible maximum power point (MPP) for switched resonant half-bridges. The theory predicts the optimal time, duration, and frequency of the energy transfers that charge the battery. Measurements of a 0.18-µm CMOS power receiver demonstrate that the receiver outputs more than 98.7% of the actual MPP at the predicted settings when the coupling factor between the transmitting and receiving coils is 0.15%–1.14%.**

***Index Terms*—Inductively coupled power receiver, maximum power-point theory, switched resonant half-bridge, wireless power transfer.**

I. Powering Embedded Microsensors

Structurally embedded microsensors and biomedical implants can sense, process, and transmit data that save energy, money, and lives [1]-[5]. Powering these microsensors is challenging because the tiny batteries that they incorporate cannot sustain their operation for long, so they need to be replenished often. Harvesting ambient energy can help, but energy sources like light or motion are rarely available in an embedded environment. Temperature gradients can also generate power, except the temperature difference across tiny devices is normally too low to generate practical power levels [6]. Often, the only option left is to transfer power wirelessly via a pair of inductively coupled coils.

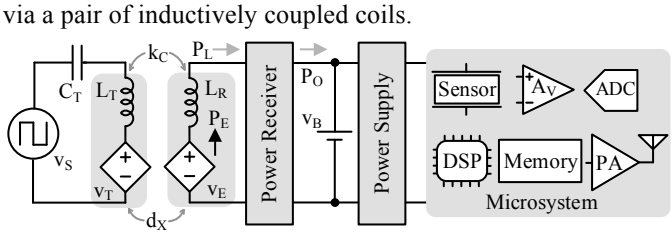

Fig. 1. Inductively powered microsystem.

To transfer power wirelessly, the transmitter's source v_S in Fig. 1 injects energy into L_TC_T. The oscillating current in L_T generates a changing magnetic field. The receiving coil L_R captures the magnetic flux that L_T emits, and induces an electromotive force (EMF) voltage v_E. To draw power, the power receiver conditions and harnesses the current from v_E. The receiver charges the battery v_B with this power so that a power supply can feed the sensor, amplifier, analog-to-digital converter (ADC), digital-signal processor (DSP), and power amplifier (PA) that comprise the microsystem.

To sustain the microsystem as long as possible, the power receiver should draw power whenever possible and output the highest power possible. Most embedded microsensors are far away (radially distant) from their transmitting sources [7]-[10], so the coupling factor k_C between the coils is very low. As a result, v_E is often tens of millivolts [11]. The only way to draw more power from such a low v_E is to raise the inductor current i_L [12]. Applying an alternating high voltage over L_R can boost i_L. Except, L_R's resistance limits this i_L [13]. The circuit's breakdown voltage, which is often only a few volts for deep submicron CMOS technologies, also limits the maximum voltage that can be applied. So the output power is both loss- and breakdown-limited [12].

This paper identifies the highest power-producing receiver in the state of the art and presents and validates (with simulations and measurements) theory that produces the highest maximum power point (MPP) possible. For this, Sections II first compares the power performance and limitations of the state of the art. Section III analyzes the highest power-producing receiver. Section IV then predicts the settings that produce the highest MPP possible. Section V validates this theory with simulations and measurements and Section VI summarizes and draws overarching conclusions.

II. Power Receivers

A. Resonant Bridge

The resonant bridge [14] in Fig. 2 parallels a resonant capacitor C_R to L_R. Since L_R and C_R resonate at v_E's operating frequency f_O, v_E constantly sources power, so the oscillation grows. As v_C grows above v_{REC}, diodes D_O^+ and D_G^+ turn on and steer i_L into C_{REC}. Similarly, as v_C grows below $-v_{REC}$, D_O^- and D_G^- turn on and steer i_L to charge up C_{REC}. v_{REC} therefore limits v_C's peak to v_{REC}.

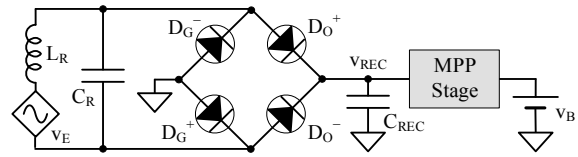

Fig. 2. Resonant bridge.

Manuscript received on October 29, 2018; revised on March 2, 2019; and accepted on March 28, 2019. The authors thank Texas Instruments (TI), Dr. Lazaro, Dr. Blanco, and Dr. Morroni for their sponsorship and support.

The authors are with the School of Electrical and Computer Engineering at the Georgia Institute of Technology, Atlanta, GA 30332-0250 U.S.A. E-mail: nxing3@gatech.edu, Rincon-Mora@gatech.edu.

In practice, D_O^-, D_G^-, D_O^+, and D_G^+ are usually comparator-based MOSFET switches because they drop millivolts [15], [16]. Ground or output diodes can be replaced with a pair of gate cross-coupled transistors to save area and power [17]. Such power receivers normally operate at megahertz. [1], [14], [16]-[18], for example, operate at 6.78 or 13.56 MHz.

The resonant bridge draws the highest power from L_R when it draws as much power as the resistance R_{ESR} in the LC tank loses [12]:

$$P_{L(MAX)} = \frac{\left(0.5v_{E(PK)}\right)^2}{2R_{ESR}}. \quad (1)$$

At this point, R_{ESR} shares $0.5v_E$ [19]. Since the reactance of C_R is Q_R times higher than R_{ESR}, the optimal capacitor voltage $v_{C(OPT)}$ is [12]:

$$v_{C(OPT)} = Q_R v_{ESR(OPT)} = 0.5Q_R v_{E(PK)}, \quad (2)$$

where Q_R is the quality factor of the LC tank.

To operate at the maximum power point (MPP), the resonant bridge requires another power stage: an MPP stage that regulates v_{REC} near $v_{C(OPT)}$. This additional stage adds losses and more components to the system. Since all four diodes see v_C, $v_{C(PK)}$ is limited to the breakdown voltage V_{BD} of the CMOS circuit. The maximum drawn power is therefore breakdown-limited when $v_{C(OPT)}$ is higher than V_{BD}.

B. Switched Bridge

Instead of using C_R, the switched bridge in Fig. 3 connects L_R to v_{REC} to raise i_L. During v_E's rising half-cycle, S_G^- and S_O^- close so v_{REC} ramps up i_L to its peak $i_{L(PK)}$. During v_E's falling half-cycle, S_G^+ and S_O^+ close, so i_L ramps down with v_E to $-i_{L(PK)}$. Since v_E is much lower than v_{REC}, i_L's waveform is triangular [12]. Although the switched bridges in [8] and [9] work at 125 kHz, the same operating principle applies at megahertz. Similarly, the switched bridge draws the most power when v_{REC} is optimal [12]:

$$P_{L(MAX)}\Big|_{v_{REC(OPT)}=0.387Q_R v_{E(PK)}} = \frac{12v_{E(PK)}^2}{\pi^4 R_{ESR}}. \quad (3)$$

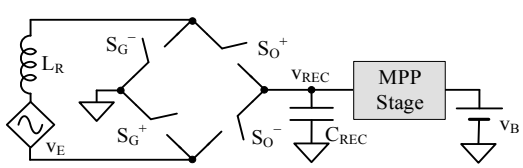

Fig. 3. Switched bridge.

For MPP, the switched bridge also needs an MPP stage to regulate v_{REC}. The circuit's V_{BD} also limits the maximum v_{REC} because all four switches see v_{REC}. To operate, the circuit needs to synchronize the switches to v_E. In [9], the switched bridge synchronizes the switches by interrupting the operation and sensing the open-circuit v_E every 11 cycles. The circuit loses 13% of its power to this interruption [9].

C. Switched Resonant Half-Bridge

The switched resonant half-bridge [10], [11], [20], [21] uses C_R to keep v_E and i_L in phase. A pair of switches, S_G (or S_C) and S_O in Fig. 4 control the energy transfer. As S_G or S_C closes, the LC tank receives power from v_E. So $v_{C(PK)}$ grows from cycle to cycle. As S_O closes and S_G (or S_C) opens, the LC tank partially transfers its energy to v_B. The switched resonant half-bridge can be categorized into two types: the series type and the parallel type. For the series type in Fig. 4a, v_B drains energy from L_RC_R in series [11]. For the parallel type in Fig. 4b, S_C opens and disconnects C_R, so v_B drains energy from L_R alone [20]. The switched resonant half-bridge can operate from 50 kHz to 6.78 MHz [10], [11], [20], [21].

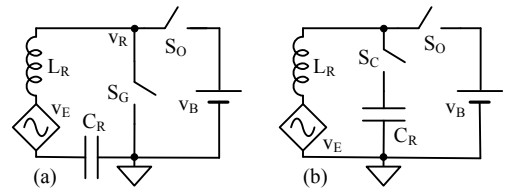

Fig. 4. Switched resonant bridges: (a) series and (b) parallel capacitors.

The switched resonant half-bridge and resonant bridge draw about the same maximum power. However, the switched resonant half-bridge does not require an MPP stage. This is because by controlling the frequency and the duration of energy transfer the circuit can adjust $v_{C(PK)}$ so it remains near $v_{C(OPT)}$. For the series type, since S_G and S_O do not see v_C, V_{BD} does not limit $v_{C(PK)}$. Yet for the parallel type, both switches S_C and S_O see v_C, so $v_{C(PK)}$ is limited to V_{BD}.

D. Comparison

When equally coupled, all three types of power receivers can output about the same power (from Eqs. 1 and 3). The switched resonant half-bridge, however, does not need the additional MPP stage that the other two require. So the switched resonant half-bridge consumes less power, and as a result, outputs more power. Between the series and parallel options, the series circuit is less breakdown-limited, so it can ultimately output more power.

III. Highest Power-Generating Receiver

Figure 5 models the series-switched resonant receiver. The transmitter couples an open-circuit voltage v_E in L_R. R_C is the reflected resistance from the transmitter [22]. As the receiver draws power, it loads the transmitter, so it lowers the current in the transmitting coil as well as v_E in L_R. The voltage dropped across R_C models this loading effect. The power receiver is modeled as a series load with a terminal voltage v_R. When S_G in Fig. 4a closes, the ground switch shorts L_R and C_R, so v_R in Fig. 5 is zero. When S_O closes, L_R is connected to v_B, so v_R equals v_B. As the circuit switches periodically, v_R's waveform is a pulse train.

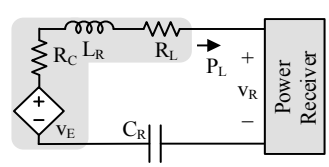

Fig. 5. Series-switched resonant power receiver.

A power stage that can adjust its energy transfer frequency, duration, and phase is proposed in [11]. This paper presents a theory that predicts the optimal (maximum power-point) settings for frequency, duration, and phase, which [11] did not include. The phase offset t_{OS} is the phase difference between v_R and v_E. When t_{OS} is zero, v_E peaks halfway across v_R's

pulse. For example, in Fig. 6, as the center of v_R's pulse lags v_E's peak by 10 ns, t_{OS} is 10 ns. The circuit can also adjust the energy-transfer frequency f_X by setting the number of cycles N_S between two consecutive transfers. In Fig. 6, as the circuit transfers energy to v_B every 5 cycles, t_X is $5t_O$ and f_X is $f_O/5$. Finally, the circuit can adjust the duration t_{ON} of the transfer: the time that the LC tank connects to v_B. In Fig. 6, v_B drains L_RC_R for 20 ns, so t_{ON} is 20 ns.

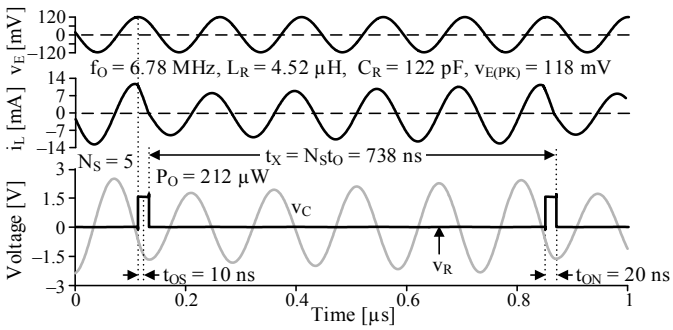

Fig. 6. Simulated waveforms of the series-switched resonant receiver.

A. Available Power

The receiver draws the highest power when the receiver load matches the source resistance $R_C + R_L$ [19]:

$$P_{L(MAX)} = \frac{\left(0.5v_{E(PK)}\right)^2}{2\left(R_L + R_C\right)}. \quad (4)$$

In practice, S_G and S_O also add resistance to the loop, lowering the maximum available power from the coupled source to:

$$P_{L(MAX)}' = \frac{\left(0.5v_{E(PK)}\right)^2}{2\left(R_C + R_L + R_{SW}\right)} = \frac{\left(0.5v_{E(PK)}\right)^2}{2R_{ESR}}. \quad (5)$$

Note the reflected R_C in Eq. (5) varies with k_C. At lower k_C, the transmitter reflects less R_C on the receiver. As a result, R_{ESR} and $P_{L(MAX)}'$ also vary with k_C.

B. Output Power

Drawing the maximum available power $P_{L(MAX)}'$ presupposes $v_{C(PK)}$ is $v_{C(OPT)}$ every cycle. However, as Fig. 6 illustrates, $v_{C(PK)}$ grows from cycle to cycle between energy transfers. $v_{C(PK)}$ therefore deviates from $v_{C(OPT)}$, so actual drawn power P_L' is lower than $P_{L(MAX)}'$. As depicted in Fig. 7, the difference between the drawn power $P_{L(i)}'$ at the i-th cycle and $P_{L(MAX)}'$ is defined as the nonlinear loss $P_{NL(i)}$, since the loss is due to the nonlinearity in the operation. As P_L' peaks parabolically at $v_{C(OPT)}$ [13], $P_{NL(i)}'$ grows quadratically with $v_{C(i)}$ deviations:

$$P_{NL(i)} = P_{L(MAX)}'\left(\frac{\Delta v_{C(i)}}{v_{C(OPT)}}\right)^2 = P_{L(MAX)}'\left(\frac{v_{C(i)} - v_{C(OPT)}}{v_{C(OPT)}}\right)^2. \quad (6)$$

The overall nonlinear loss P_{NL} is the average over N_S cycles:

$$P_{NL} = P_{NL(AVG)} = \frac{1}{N_S}\sum_{i=1}^{N_S} P_{NL(i)} = \frac{1}{N_S}\sum_{i=1}^{N_S}\left(P_{L(MAX)}' - P_{L(i)}'\right). \quad (7)$$

P_{NL} is lowest when $v_{C(PK)}$'s (from Fig. 7) average $v_{C(OPT)}$.

The circuit also loses charge power as parasitic capacitances charge and discharge. This charge loss P_C is proportional to f_X:

$$P_C = v_{DD}q_Cf_X = v_{DD}^2k_{SW}C_{EQ}f_X, \quad (8)$$

where C_{EQ} is the total equivalent capacitance that charges and discharges in one switching cycle. k_{SW} is the soft-switching

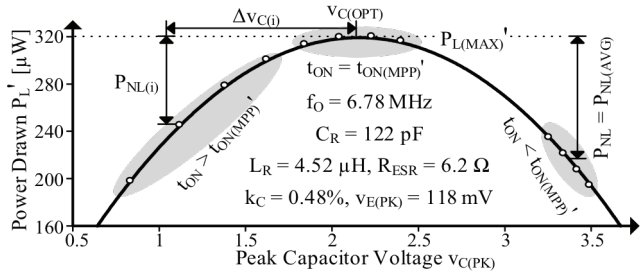

Fig. 7. Drawn power and resulting nonlinear loss.

factor. Without t_{DT}, M_O hard-switches: burns power to charge v_{SW}'s parasitic capacitance C_{EQ}, so k_{SW} = 1. With t_{DT}, L_X's current charges C_{EQ} before M_O closes, so M_O partially soft-switches: closes with lower than v_B voltage drop. L_X's current also charges C_{EQ} above v_B before M_G closes, so M_G switches with higher charge loss. As a result, k_{SW} can be higher or lower than 1. The analysis assumes k_{SW} = 1. The accuracy of this assumption will be verified by simulations and measurements later. Output power P_O is the $P_{L(MAX)}'$ that nonlinear and charge losses P_{NL} and P_C avail:

$$P_O = P_{L(MAX)}' - P_{NL} - P_C. \quad (9)$$

IV. Maximum Power

The theory below finds MPP settings $t_{OS(MPP)}$, $t_{ON(MPP)}$, and $f_{X(MPP)}$ in two steps. The theory first finds the optimal t_{OS} and t_{ON} settings that maximize P_O at a given f_X. The optimal settings derived $t_{OS(MPP)}'$ and $t_{ON(MPP)}'$ are "local" because they vary with f_X. As will be shown, $t_{OS(MPP)}'$ and $t_{ON(MPP)}'$ are the t_{OS} and t_{ON} that ensure $v_{R(PK)}$'s f_O^{th} harmonic is $0.5v_{E(PK)}$. The optimal "global" setting derived for f_X in step two ($f_{X(MPP)}$) minimizes the losses at this point: when $v_{R(PK)}^{fO}$ is $0.5v_{E(PK)}$. With this, the optimal global setting for t_{ON} ($t_{ON(MPP)}$) is now known: from $t_{ON(MPP)}'$ in step one and $f_{X(MPP)}$ in step two.

A. Optimal Receiver Voltage

Ideally, the power receiver in Fig. 5 outputs the highest power when the receiver load matches R_{ESR}, so v_R is $0.5v_E$. In reality, v_R is not a sinusoidal wave but a pulse train with a frequency f_X that is f_O/N_S. Fourier series decomposes v_R as the sum of sinusoidal waveforms at f_X and its harmonics. The N_S-th harmonic of v_R is at f_O. Since the series L_RC_R only band passes current at f_O, v_R's harmonic at f_O dominates the current and the conduction loss. Therefore, analogous to the linear maximum power transfer theory [19], the proposed theory asserts that at given f_X the receiver draws maximum power when v_R's harmonic at f_O matches $0.5v_E$ in both amplitude and phase:

$$v_{R(PK)}^{(f_O)} = 0.5v_{E(PK)},\ \angle v_R^{(f_O)} = \angle v_E. \quad (10)$$

Expanding v_R's Fourier series at f_O relates $t_{ON(MPP)}'$ and t_X:

$$v_{R(PK)}^{(f_O)} = \left(\frac{2}{\pi}\right)\left(\frac{f_X}{f_O}\right)v_B \sin\left[\pi\left(\frac{t_{ON}}{t_O}\right)\right]\Bigg|_{t_{ON(MPP)}'} = \frac{v_{E(PK)}}{2}. \quad (11)$$

Solving (11) gives the local $t_{ON(MPP)}'$ at given f_X:

$$t_{ON(MPP)}' = \left(\frac{t_O}{\pi}\right)\sin^{-1}\left[\left(\frac{\pi}{4}\right)\left(\frac{v_{E(PK)}}{v_B}\right)\left(\frac{f_O}{f_X}\right)\right]. \quad (12)$$

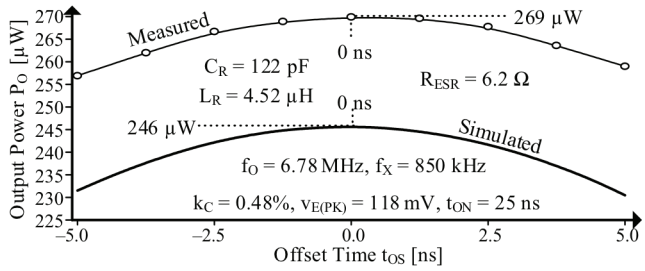

Fig. 8. Output power across offset time.

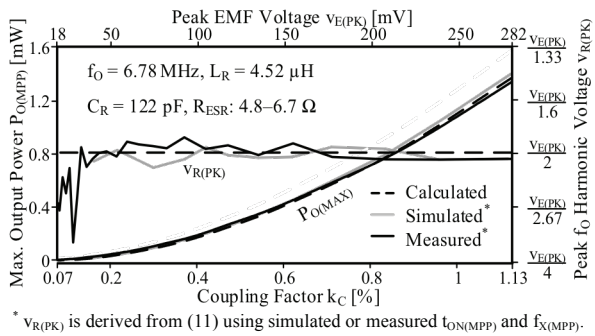

* $v_{R(PK)}$ is derived from (11) using simulated or measured $t_{ON(MPP)}$ and $f_{X(MPP)}$.

Fig. 9. Maximum output power and receiver's peak f_O harmonic voltage.

From (11), since v_R's harmonic at f_O and v_E are in phase, the center of the pulse aligns with v_E's peak. Therefore, the phase offset at the local and the global MPP is zero:

$$t_{OS(MPP)}' = t_{OS(MPP)} = 0. \tag{13}$$

Fig. 8 plots the simulated and measured P_O across t_{OS} when f_X = 850 kHz and t_{ON} = 25 ns. In both simulation and measurement, the circuit outputs the highest power when t_{OS} = 0. P_O drops as t_{OS} deviates from zero in either direction. Fig. 9 plots the calculated, simulated, and measured $V_{R(PK)}^{(f_0)}$ at MPP when k_C is 0.07–1.13%. At k_C > 0.15%, both simulated and measured $V_{R(PK)}^{(f_0)}$ is within 4% of $0.5v_{E(PK)}$, corroborating the theory well. However, when k_C is less than 0.15%, the measured $V_{R(PK)}^{(f_0)}$ deviates up to 21% from $0.5v_{E(PK)}$, due to the finite resolutions for t_{ON} and f_X (5 ns and 53 kHz, respectively).

Fig. 10 plots the simulated and measured P_O across t_{ON} when $f_X = 0.125f_O$. The simulated P_O peaks at t_{ON} = 23 ns, deviating 1 ns from the theory's predicted 24 ns. The measured P_O peaks at t_{ON} = 25 ns with 5 ns resolution. Simulated k_{SW} ranges from 0.86% to 1.14%. To evaluate the accuracy of the predicted $t_{ON(MPP)}'$ in (12), Fig. 11 compares the calculated, simulated, and measured $t_{ON(MPP)}'$ across f_X with 118 mV of $v_{E(PK)}$ and 6.2 Ω of R_{ESR}. While the simulated $t_{ON(MPP)}'$ closely matches the theory' prediction, the measured $t_{ON(MPP)}'$ has a resolution of 5 ns and reflects the trend of prediction.

B. Optimal Transfer Frequency

The next step for MPP is to find the optimal f_X that maximizes the global P_O with the corresponding $t_{OS(MPP)}'$ and $t_{ON(MPP)}'$ found in the previous step. For this, as discussed in Section III, f_X needs to minimize the total losses P_{NL} + P_C. Between energy transfers, the LC tank collects across cycles the power L_R sources. The difference between consecutive cycles i – 1

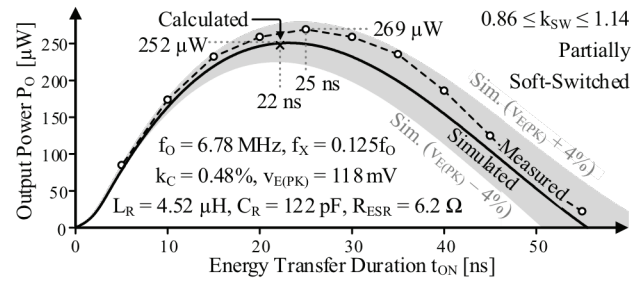

Fig. 10. Output power across duration.

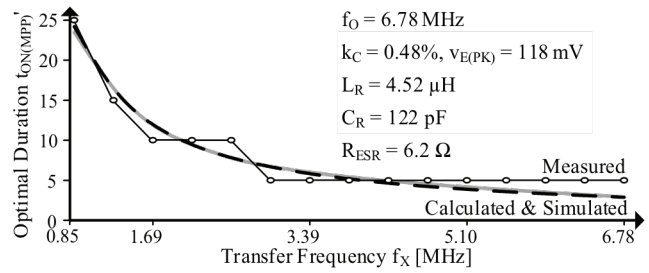

Fig. 11. Optimal duration.

and i's peak C_R energy, therefore, reflects energy the L_R sources across cycle i [13]:

$$P_{L(i)}'t_O = E_{C(i)} - E_{C(i-1)} = 0.5C_R\left(v_{C(i)}^2 - v_{C(i-1)}^2\right). \tag{14}$$

$P_{L(i)}'$ is the difference between $P_{L(MAX)}'$ and $P_{NL(i)}'$, so according to (6) and (7):

$$P_{L(i)}' = P_{L(MAX)}' - P_{NL(i)} = P_{L(MAX)}'\left[1-\left(\frac{v_{C(i)} - v_{C(OPT)}}{v_{C(OPT)}}\right)^2\right]. \tag{15}$$

Replacing $P_{L(i)}'$ in (14) with (15), $v_{C(PK)}$ can be calculated iteratively from cycle to cycle:

$$v_{C(i)} \approx \pi v_{E(PK)} + v_{C(i-1)}\left(1-\frac{\pi}{Q_R}\right). \tag{16}$$

Assume $v_{C(PK)}$ is closest to $v_{C(OPT)}$ at the m-th cycle, using (16), $v_{C(PK)}$ at i-th cycle can be calculated as:

$$v_{C(i)} = 2v_{C(OPT)} - v_{C(OPT)}\left(1-\frac{\pi}{Q_R}\right)^{i-m}. \tag{17}$$

Replacing $v_{C(i)}$ in (6) with (17) and assuming P_O is locally maximized, P_{NL} at the local MPP can be expressed as:

$$P_{NL(MPP)}' = P_{L(MAX)}'\left[1-\left(\frac{4a}{1-a^2}\right)\left(\frac{1-a^{f_O/f_X}}{1+a^{f_O/f_X}}\right)\left(\frac{f_X}{f_O}\right)\right], \tag{18}$$

where $a = 1-\frac{\pi}{Q_R}$. Since P_C is not a function of t_{OS} or t_{ON}, $P_{C(MPP)}' = P_C$ at f_X. As Fig. 12 shows, the theory predicts P_{NL}, P_C, and thus P_O at the local MPP. For global MPP, $f_{X(MPP)}$ needs to minimize the total losses $P_{NL(MPP)}'$ + P_C:

$$\frac{\delta P_{O(MPP)}'}{\delta f_X} = -\frac{\delta P_{NL(MPP)}'}{\delta f_X} - \left.\frac{\delta P_C}{\delta f_X}\right|_{f_{X(MPP)}} = 0. \tag{19}$$

With the $P_{NL(MPP)}'$ obtained in (18) and P_C obtained in (8), solving (19) gives $f_{X(MPP)}$:

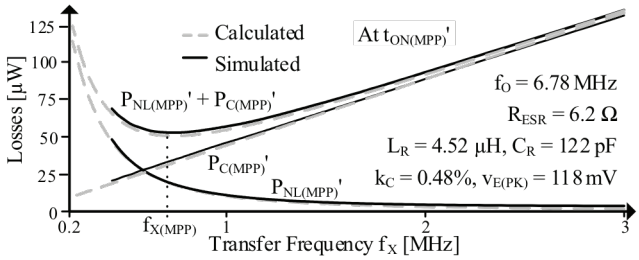

Fig. 12. Losses and resulting optimal transfer frequency.

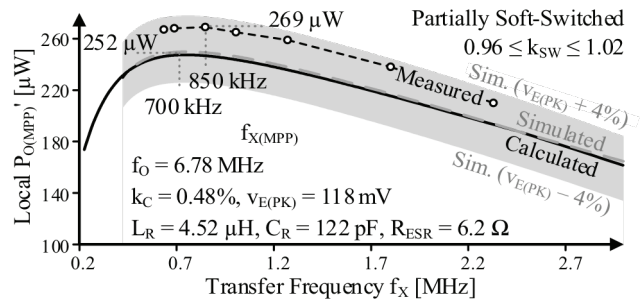

Fig. 13. Optimized output power.

$$f_{X(MPP)} = f_O \left[\left(\frac{\pi}{2Q_R} \right)^2 \left(\frac{P_{L(MAX)}'}{P_{C(f_O)}} \right) \right]^{1/3}, \tag{20}$$

where $P_{C(f_O)}$ is the charge loss when $f_X = f_O$. The global optimal $t_{ON(MPP)}$ is, therefore, $t_{ON(MPP)}'$ at $f_{X(MPP)}$:

$$t_{ON(MPP)} = t_{ON(MPP)}'\Big|_{f_X = f_{X(MPP)}}. \tag{21}$$

Detailed derivations of (16), (17), (18), and (20) are included in the Appendix. Fig. 12 compares the simulated losses with the theory's prediction in (8) and (18). The theory accurately predicts the simulated P_{NL} and P_C with less than 5% error when f_X is 420 kHz–3MHz.

C. Maximum Output Power

With the losses (P_{NL} and P_C) and MPP settings ($t_{OS(MPP)}$, $t_{ON(MPP)}$, $f_{X(MPP)}$) obtained in the previous two subsections, the output power is $P_{L(MAX)}'$ minus the losses at the MPP settings:

$$P_{O(MPP)} = P_{L(MAX)}' - P_{NL(MPP)} - P_{C(MPP)} \tag{22}$$

Fig. 13 compares the calculated, simulated, and measured P_O across f_X at 118 mV of $v_{E(PK)}$ and 6.2 Ω of R_{ESR}. Testing accuracy and measurement noise produce an error. With up to ±5 mV of resolution and noise errors, measured v_E is up to ±4% off, which means calculated and simulated projections are off by a corresponding amount. Figs. 10 and 13 show that measured data is within the projected error window. The hard-switching assumption in the calculations also contributes error. But like Fig. 12 shows, calculations and simulations match, so this error is small. At the theory's predicted $f_{X(MPP)}$ of 700 kHz, the measured P_O is only 1% lower than the actual $P_{O(MPP)}$.

V. Validation

A. Prototype

To validate the theory, a series switched resonant half-bridge power receiver prototype is built in 180 nm CMOS technology. The dead time logic in Fig. 14 inserts delays to

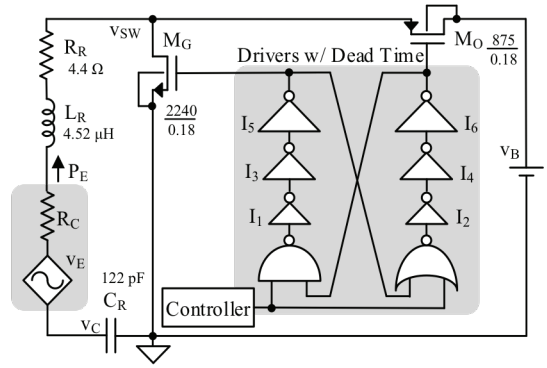

Fig. 14. Prototype of the series-switched resonant power receiver.

prevent M_G and M_O from turning on at the same time and shorting v_B to the gro und. The receiver prototype uses an off-chip coil PA6512-AE from Coilcraft that measures 4.52 µH. The integrated resonant capacitor C_R is laser trimmed to 122 pF with ±1-pF accuracy. L_R and C_R resonate at 6.78 MHz.

The prototype IC in Fig. 15 occupies 644 µm × 732 µm of area. The linear stage in Fig. 15 adjusts the distance d_X between the coils from 13 mm to 38 mm, so k_C is 0.07%–1.13%. Although separation is 38 mm, the coils are 4.5 radial lengths apart (where radial lengths refers to the radii of the coils), which is as far apart as some of the best inductively coupled systems can output power, like in [16], [18], [21], [24]. This 38-mm (power) transmission distance is suitable for implanted biosensors like glucose and blood-pressure sensors, since such sensors are typically implanted underneath the skin [1], [3]. The corresponding R_C varies 0–1.9 Ω, so the total R_{ESR} varies 4.8–6.7 Ω. An FPGA controls t_{OS}, t_{ON} and f_X of the power receiver with 1.25 ns, 5 ns, and 53 kHz of resolution, respectively.

B. Calculation

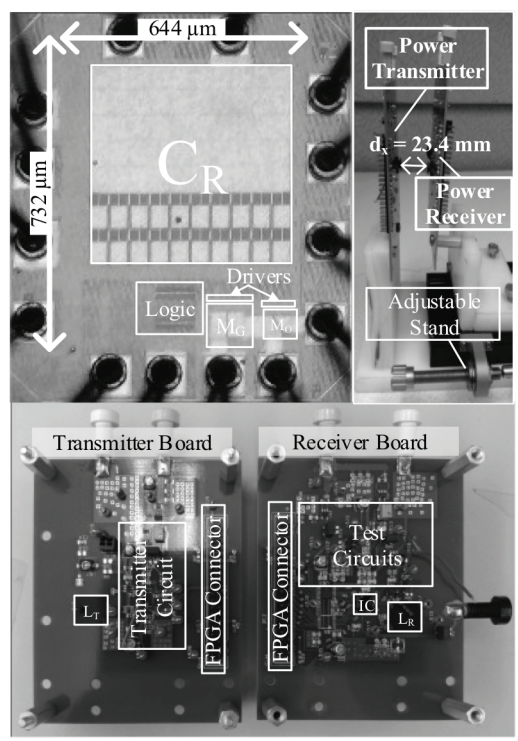

Fig. 15. 180-nm CMOS die, measurement setup, and system top view.

The equivalent charge loss capacitance C_{EQ} includes the M_G gate capacitance C_{GN}, M_O's gate capacitance C_{GP}, M_O's source to well junction capacitance C_{JSW}, and M_G's drain to substrate junction capacitance C_{JDSUB}:

$$C_{GN} = C_{OX}''W_N L_N = 3.7\,\text{pF}. \tag{23}$$

$$C_{GP} = C_{OX}''W_P L_P = 1.4\,\text{pF}. \tag{24}$$

$$C_{JSW} = \frac{C_{J0}''A_{SW}}{\sqrt{1 - v_D / v_{BI}}} = 0.14\,\text{pF}. \tag{25}$$

$$C_{JDSUB} = \frac{C_{J0}''A_{DSUB}}{\sqrt{1 - v_D / v_{BI}}} = 0.37\,\text{pF}. \tag{26}$$

C_{EQ} also includes parasitic capacitance at the pins and the pads, which can be estimated from process and datasheets. The total C_{EQ} is estimated as:

$$\begin{aligned} C_{EQ} &= C_{PIN} + C_{PAD} + C_{JDSUB} + C_{JSW} \\ &+ (2^2+1)(0.5C_{GN}) + (2^2+1)(0.5C_{GP}) = 18.2\,\text{pF} \end{aligned}. \tag{27}$$

Note as the voltage swing across the C_{GD} (~$0.5C_{GN}$) of M_G and C_{GS} (~$0.5C_{GP}$) of M_O doubles v_B, their equivalent capacitance counts four times as much. In total, C_{EQ} includes 2.5 times of C_{GN} and C_{GP}.

Table I summarizes the parameters, design variables and implied power in calculation, simulation, and measurement. Since the MOSFET models are no longer available from the manufacturer after the IC is fabricated, the parameters for simulations are chosen such that the simulated R_{SWN}, R_{SWP}, and
C_{EQ} closely match the calculation. Measured R_{SWN} and R_{SWP} are higher than estimated values, so the available power $P_{L(MAX)}'$ is 1.3–1.7% lower. The measured $P_{C(f_O)}$ is 12% lower than the estimated value. However, the mismatch in R_{ESR}, $P_{L(MAX)}'$, and $P_{C(f_O)}$ only causes 4% error in $f_{X(MPP)}$ according to (20).

C. Simulations

To evaluate P_O, the simulation monitors the average net current into v_B. P_L' can be obtained from L_R's voltage and current. The simulation estimates the ohmic loss P_R on R_{ESR} from the i_L waveform. P_L' minus P_O and P_R gives the charge loss P_C.

Fig. 16 plots the simulated and measured P_O over the variable space by sweeping t_{ON} and f_X with 5 ns and 53 kHz of resolution, respectively. The measured P_O maximizes at 269 μW when t_{ON} = 25 ns. The FPGA controller cannot respond within 5 ns, so 5 ns is the practical limit. Higher bandwidth is not necessary because, as Fig. 16 shows, P_O is not very sensitive to t_{ON} near P_O's maximum power point: P_O varies 2% with ±5-ns variations in t_{ON}.

D. Measurements

The induced v_E is measured as the open-circuit voltage across L_R. R_C models the receiver's damping effect on the transmitter's reflected source. So when short-circuiting v_E and R_C, R_C consumes the same power that v_S supplies when the transmitter is unloaded. $v_{E(PK)}$ and R_C in measurements are therefore L_R's peak open-circuit voltage and the equivalent resistance that burns v_S's power when the transmitter is unloaded [11]. Efficiency is 12%–59% when the coupling coefficient k_C is 0.07%–1.13%. This is okay because the aim is to maximize P_O (not efficiency), so that P_O is at its MPP.

TABLE I: PARAMETER SUMMARY

Parameters			
Parameter	**Value**	**Parameter**	**Value**
f_O	6.78 MHz	$v_{E(PK)}$	18–282 mV
k_C	0.07–1.13%	L_R	4.52 μH
C_R	122 pF	R_L	4.4 Ω
Design Variables			
	Calculated	**Simulated**	**Measured**
R_{SWN}	0.37 Ω		0.45 Ω
R_{SWP}	3.7 Ω		5 Ω
C_{EQ}	18.2 pF		16.5 pF
Implied Power			
	Calculated	**Simulated**	**Measured**
$P_{L(MAX)}$	9.2–1580 μW		
$P_{L(MAX)}'$	8.5–1490 μW*		8.4–1470 μW*
$P_{C(f_O)}$	280 μW		252 μW

*$P_{L(MAX)}'$ is derived from (5) with calculated, simulated, and measured R_{ESR}.

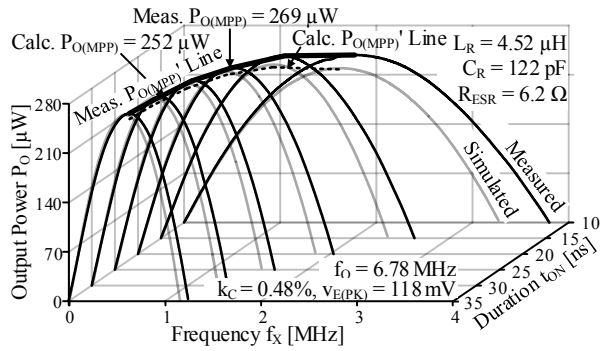

Fig. 16. Variable space for output power.

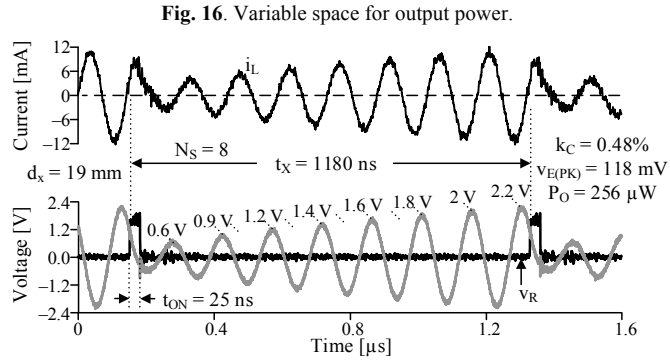

Fig. 17. Measured waveforms.

Fig. 17 shows the measured waveforms of v_C, i_L, and v_R at 118 mV of induced v_E. The receiver transfers power to v_B for 25 ns every 8 cycles. Fig. 18 compares the calculated, simulated and measured $t_{ON(MPP)}$ and $N_{S(MPP)}$. The calculated and simulated $t_{ON(MPP)}$ and $f_{X(MPP)}$ are rounded up to the closest 5 ns or 53 kHz to match the measurement resolution. The simulated and measured $t_{ON(MPP)}$ are often 5–10 ns higher than the theory's prediction. The simulated and measured $N_{S(MPP)}$ are often higher as well. Fig. 19 compares the measured P_O at the theory's predicted MPP settings with the actual $P_{O(MPP)}$. The MPP error denotes the percentage difference between P_O at the predicted MPP setting and the actual $P_{O(MPP)}$. The circuit outputs 344 μW halfway across the coupling k_C range tested, which is sufficient for microsensor applications such as blood-pressure and glucose sensors [1] and [3].

E. Deviation

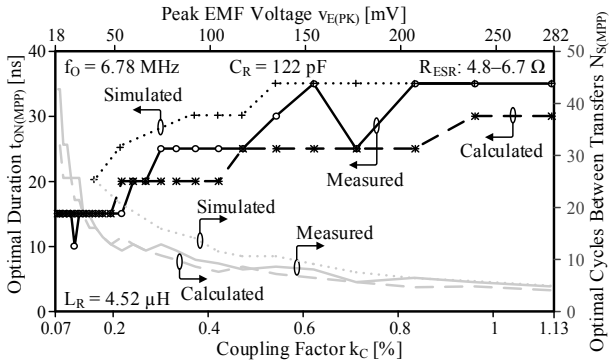

Fig. 18. Optimal duration and number of cycles between transfers.

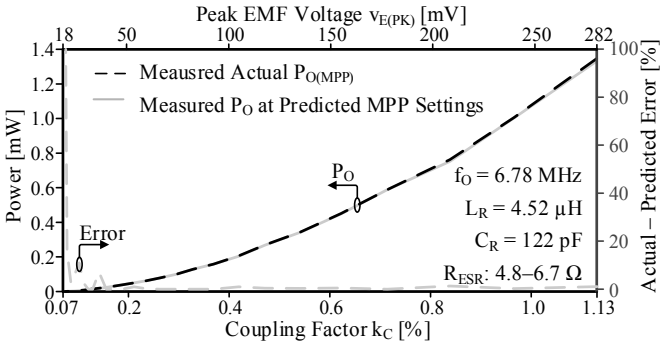

Fig. 19. P_O at the predicted MPP setting and the actual MPP setting

Table II summarizes and compares the calculated MPP settings and power with simulation and measurement when k_C > 0.15%. The theory's predicted $t_{ON(MPP)}$ is 17–30% lower than the simulation and 2–24% lower than the measurement, while the predicted $f_{X(MPP)}$ is 21–66% higher than the simulation and 2–32% higher than the measurement. Testing accuracy and noise produces an error in v_E that, along with the approximations in (35) and (38), offsets projected $f_{X(MPP)}$, and by translation, $t_{ON(MPP)}$ from their actual values by up to –30% and +66%. P_O, however, is still within 1.3% of its maximum power point $P_{O(MPP)}$ because P_O (in Fig. 16) is fairly insensitive to settings near $P_{O(MPP)}$. These inaccuracies in $f_{X(MPP)}$ and $t_{ON(MPP)}$ are therefore acceptable. In practice, rather than the accuracy of the MPP settings, it is more important that P_O at the predicted setting is as close to the actual $P_{O(MPP)}$ as possible, so the MPP error is low. The MPP error is within 3.8% for simulation and within 1.3% for measurement. Since the series switched resonant half-bridge outputs as much or more power than other receivers, the $P_{O(MPP)}$ theorized here is also the highest $P_{O(MPP)}$ a receiver can output.

[10], [23]-[25] explored maximum end-to-end efficiency (MPE) for strongly coupled switched resonant bridges and half bridges. When weakly coupled, the receiver barely loads the transmitter [11], so the maximum power point (MPP) is also the MPE. Theorized MPEs in [23]-[25] fix f_X at $2f_O$, which is not optimal because switching (charge) losses are not minimized this way [13], and the MPE is not global. Although [10] varies f_X, it does not account for these switching losses. Plus, [10] linearizes the operation of the circuit, which means [10] also discounts the nonlinear effects of the multi-cycle switching system. This paper shows that both losses are significant when weakly coupled, and shows how these losses can be minimized. More generally, the theory proposed here adjusts all variables and accounts for all losses to ensure the MPP is global and the highest possible.

TABLE II: MPP SETTINGS SUMMARY

Parameter*	Calculated	Simulated		Measured	
		Value	Error	Value	Error
$t_{OS(MPP)}$	0	0	0%	0	0%
$t_{ON(MPP)}$	16–29 ns	15–35 ns	–(17%–30%)	15–35 ns	–(2%–24%)
$f_{X(MPP)}$	0.44–1.7 MHz	0.26–1.4 MHz	21%–66%	0.43–1.4 MHz	2%–32%
Actual $P_{O(MPP)}$		13–1400 µW		24–1350 µW	
Predicted $P_{O(MPP)}$		13–1380 µW		24–1330 µW	
MPP Error		< 3.8%		< 1.3%	

VI. CONCLUSIONS

This paper explores and theorizes the MPP operation of the switched resonant half-bridge power receiver. The theory predicts the optimal phase, duration, and frequency of energy transfer in a closed form fashion. To prove the theory, a power receiver prototype is fabricated in 0.18 µm CMOS technology. Measurements show that at the theory's predicted settings, the receiver outputs more than 98.7% of the actual maximum power when the coupling is 0.15%–1.13%.

APPENDIX OPTIMAL DERIVATIONS

A. Peak Capacitor Voltage

Combining (14) and (15) yields:

$$0.5C_R\left(v_{C(i+1)}-v_{C(i)}\right)\left(v_{C(i+1)}+v_{C(i)}\right) = P_{L(MAX)}'\left[\frac{v_{C(i)}\left(2v_{C(OPT)}-v_{C(i)}\right)}{v_{C(OPT)}^{2}}\right]t_O. \quad (28)$$

Since the quality factor Q_R of the LC is normally much greater than one, oscillation growth from cycle to cycle is slow. Assuming $v_{C(i+1)} + v_{C(i)} \approx 2v_{C(i)}$, (28) can be simplify ed as:

$$v_{C(i+1)}-v_{C(i)} = \left(\frac{t_O P_{L(MAX)}'}{2C_R v_{C(OPT)}^{2}}\right)\left(2v_{C(OPT)}-v_{C(i)}\right). \quad (29)$$

Replacing $P_{L(MAX)}'$ and $v_{C(OPT)}$ with expressions in (2) and (5) yields (18). Also, equation (18) can be re-written as:

$$v_{C(i+1)}-2v_{C(OPT)} = \left(1-\frac{\pi}{Q_R}\right)\left(v_{C(i)}-2v_{C(OPT)}\right). \quad (30)$$

With (30), $v_{C(PK)}$ can be iteratively calculated as in (17).

B. Nonlinear Loss

Replacing $v_{C(i)}$ in (6) with (17), $P_{NL(i)}$ can be expressed as:

$$P_{NL(i)} = P_{L(MAX)}'\left(1-a^{i-m}\right)^2. \quad (31)$$

Substituting $P_{NL(i)}$ in (7) with (31) gives the closed form P_{NL}:

$$P_{NL} = \frac{1}{N_S}\sum_{i=1}^{N_S} P_{L(MAX)}'\left(1-2a^{i-m}+a^{2i-2m}\right) = P_{L(MAX)}'\left[1-\frac{2a^{-m}}{N_S}\left(\frac{1-a^{N_S}}{1-a}\right)+\frac{a^{-2m}}{N_S}\left(\frac{1-a^{2N_S}}{1-a^2}\right)\right]. \quad (32)$$

At the local maximum point, intuitively, $v_{C(PK)}$ centers around $v_{C(OPT)}$. Therefore, it is fair to assume the nonlinear loss of the first cycle approximately equals that of the last cycle:

$$P_{NL(1)} \approx P_{NL(N_S)}, \tag{33}$$

which gives:

$$P_{L(MAX)}'\left(1-a^{1-m}\right)^2 \approx P_{L(MAX)}'\left(1-a^{N_S-m}\right)^2. \tag{34}$$

Simplifying (34) yields:

$$a^{-m} \approx \frac{2}{a+a^{N_S}} \approx \frac{2}{1+a^{N_S}}. \tag{35}$$

Substituting a^{-m} in (32) with (35), P_{NL} at the local maximum point can be re-written as:

$$P_{NL(MPP)}' = P_{L(MAX)}'\left[1-\left(\frac{4a}{1-a^2}\right)\left(\frac{a^{-0.5N_S}-a^{0.5N_S}}{a^{-0.5N_S}+a^{0.5N_S}}\right)\left(\frac{1}{N_S}\right)\right]. \tag{36}$$

Equation (18) can be easily derived from (36).

C. Skipped Cycles

Expanding (19) with expressions in (8) and (18) yields:

$$P_{L(MAX)}'\left(\frac{2a}{1+a}\right)\frac{(-\ln a)\left(a^{-0.5N_S}-a^{0.5N_S}\right)}{\left(a^{-0.5N_S}+a^{0.5N_S}\right)^2} = \frac{P_{C(f_O)}}{N_S^{\,2}}. \tag{37}$$

Again, since Q_R is normally much greater than one, a is close to one. Using Taylor expansion, the following terms in (37) can be approximated and simplified as:

$$a^{-0.5N_S}+a^{0.5N_S} \approx 2, \quad \frac{\left(a^{-0.5N_S}-a^{0.5N_S}\right)}{N_S} \approx 1-a. \tag{38}$$

With the approximation, (36) can be simplified as:

$$P_{L(MAX)}'\left(\frac{2a}{1+a}\right)\frac{(-\ln a)N_S(1-a)}{4} \approx \frac{P_{C(f_O)}}{N_S^{\,2}}. \tag{39}$$

Again, use Taylor expansion to approximate the term in (39):

$$-\ln a = \ln\left[1+\left(\frac{1}{a}-1\right)\right] \approx \frac{1-a}{a}. \tag{40}$$

Solving (39) with the approximation in (40) yields the optimal number of cycles N_S between energy transfers:

$$N_S^{\,3} \approx \left(\frac{4P_{C(f_O)}}{P_{L(MAX)}'}\right)\left(\frac{Q_R}{\pi}\right)^2. \tag{41}$$

From (41), $f_{X(MPP)}$ can be easily obtained as in (20).

REFERENCES

[1] M. M. Ahmadi and G. A. Jullien, "A wireless-implantable microsystem for continuous blood glucose monitoring," *IEEE Transactions on Biomedical Circuits and Systems,* vol. 3, pp. 169-180, 2009.

[2] A. D. DeHennis and K. D. Wise, "A wireless microsystem for the remote sensing of pressure, temperature, and relative humidity," *Journal of Microelectromechanical Systems,* vol. 14, pp. 12-22, February 2005.

[3] C. Peng, W. H. Ko, and D. J. Young, "Wireless batteryless implantable blood pressure monitoring microsystem for small laboratory animals," *IEEE Sensors Journal,* vol. 10, pp. 243-54, February 2010.

[4] P.-J. Chen, S. Saati, R. Varma, M. S. Humayun, and Y.-C. Tai, "Wireless intraocular pressure sensing using microfabricated minimally invasive flexible-coiled LC sensor implant," *Journal of Microelectromechanical Systems,* vol. 19, pp. 721-34, August 2010.

[5] H. Marques, B. Borges, P. Ramos, and A. Martins, "Contactless battery charger for composite humidity and temperature wireless sensors," *International Conference on Computer as a Tool*, pp. 1-4, April 2011.

[6] E. O. Torres and G. A. Rincon-Mora, "Energy-harvesting system-in-package microsystem," *Journal of Energy Engineering,* vol. 134, pp. 121-9, 12/ 2008.

[7] O. Lazaro and G. A. Rincon-Mora, "180-nm CMOS wideband capacitor-free inductively coupled power receiver and charger," *IEEE Journal of Solid-State Circuits,* vol. 48, pp. 2839-49, November 2013.

[8] O. Lazaro and G. A. Rincon-Mora, "Inductively coupled 180-nm CMOS charger with adjustable energy-investment capability," *IEEE Transactions on Circuits and Systems II: Express Briefs,* vol. 60, pp. 482-6, August 2013.

[9] O. Lazaro and G. A. Rincon-Mora, "A nonresonant self-synchronizing inductively coupled 0.18-m CMOS power receiver and charger," *IEEE Journal of Emerging and Selected Topics in Power Electronics,* vol. 3, pp. 261-271, January 2015.

[10] H. S. Gougheri and M. Kiani, "Current-based resonant power delivery with multi-cycle switching for extended-range inductive power transmission," *IEEE Transactions on Circuits and Systems I: Regular Papers,* vol. 63, pp. 1543-52, September 2016.

[11] N. Xing and G. A. Rincón-Mora, "180-nm 85%-efficient inductively coupled switched resonant half-bridge power receiver," *IEEE Transactions on Circuits and Systems II: Express Briefs,* to be published, 10.1109/TCSII.2018.2867795.

[12] N. Xing and G. A. Rincon-Mora, "Generating the highest power with a tiny and distant inductively coupled coil," *IEEE International Symposium on Industrial Electronics*, pp. 477-80, June 2016.

[13] N. Xing and G. A. Rincon-Mora, "Power analysis and maximum output-power scheme for inductively coupled resonant power receivers," *IEEE International Midwest Symposium on Circuits and Systems*, pp. 293-6, August 2017.

[14] K. G. Moh, F. Neri, S. Moon, P. Yeon, J. Yu, Y. Cheon*, et al.*, "A fully integrated 6W wireless power receiver operating at 6.78MHz with magnetic resonance coupling," *IEEE International Solid-State Circuits Conference*, pp. 230-232, February 2015.

[15] J. Charthad, M. J. Weber, T.-C. Chang, and A. Arbabian, "A mm-sized implantable medical device (IMD) with ultrasonic power transfer and a hybrid bi-directional data link," *IEEE Journal of Solid-State Circuits,* vol. 50, pp. 1741-53, August 2015.

[16] X. Li, C.-Y. Tsui, and W.-H. Ki, "A 13.56 MHz wireless power transfer system with reconfigurable resonant regulating rectifier and wireless power control for implantable medical devices," *IEEE Journal of Solid-State Circuits,* vol. 50, pp. 978-89, April 2015.

[17] H. Cheng, T. Kawajiri, and H. Ishikuro, "A near-optimum 13.56 MHz CMOS active rectifier with circuit-delay real-time calibrations for high-current biomedical implants," *IEEE Journal of Solid-State Circuits,* vol. 51, pp. 1797-809, August 2016.

[18] S. B. Lee, H.-M. Lee, M. Kiani, U.-M. Jow, and M. Ghovanloo, "An inductively powered scalable 32-channel wireless neural recording system-on-a-chip for neuroscience applications," *IEEE Transactions on Biomedical Circuits and Systems,* vol. 4, pp. 360-371, 2010.

[19] C. S. Kong, "A general maximum power transfer theorem," *IEEE Transactions on Education,* vol. 38, pp. 296-298, March 1995.

[20] M. Choi, T. Jang, J. Jeong, S. Jeong, D. Blaauw, and D. Sylvester, "A resonant current-mode wireless power receiver and battery charger with -32 dBm sensitivity for implantable systems," *IEEE Journal of Solid-State Circuits,* vol. 51, pp. 2880-92, December 2016.

[21] M. Kiani, L. Byunghun, Y. Pyungwoo, and M. Ghovanloo, "A power-management ASIC with Q-modulation capability for efficient inductive power transmission," *IEEE International Solid-State Circuits Conference*, pp. 226-8, Feburary 2015.

[22] S. Y. R. Hui, W. Zhong, and C. K. Lee, "A Critical Review of Recent Progress in Mid-Range Wireless Power Transfer," *IEEE Transactions on Power Electronics,* vol. 29, pp. 4500-4511, 2014.

[23] B. X. Nguyen, D. M. Vilathgamuwa, G. H. B. Foo, P. Wang, A. Ong, U. K. Madawala*, et al.*, "An efficiency optimization scheme for bidirectional inductive power transfer systems," *IEEE Transactions on Power Electronics,* vol. 30, pp. 6310-19, November 2015.

[24] M. Kiani, B. Lee, P. Yeon, and M. Ghovanloo, "A Q-modulation technique for efficient inductive power transmission," *IEEE Journal of Solid-State Circuits,* vol. 50, pp. 2839-2848, December 2015.

[25] K. Colak, E. Asa, M. Bojarski, D. Czarkowski, and O. C. Onar, "A novel phase-shift control of semibridgeless active rectifier for wireless power transfer," *IEEE Transactions on Power Electronics,* vol. 30, pp. 6288-97, November 2015.

Nan Xing (SM'16) is currently working toward the Ph.D. degree in Georgia Tech Analog, Power, and Energy IC Lab. From 2010 to 2013, he was a mixed signal IC design engineer at Samsung Electronics, Yongin. He was the recipient of Samsung Global Scholarship (2008-2010) and Brain Korea 21 Research Award (2010).

Gabriel A. Rincón-Mora (StM'90, GSM'93, M'97, SM'01, F'11) is a Professor at Georgia Tech, Fellow of the National Academy of Inventors and Fellow of the Institution of Engineering and Technology. He authored 9 books, 1 handbook, 4 book chapters, 42 patents, over 180 articles.